Mechanical Response of 3D Printed Bending-Dominated Ligament-Based Triply Periodic Cellular Polymeric Solids

Aliaa M. Abou-Ali, Oraib Al-Ketan, Reza Rowshan, and Rashid Abu Al-Rub

Lightweight materials with complex structures such as cellular solids (or foams) have proven to possess desirable properties, specifically in terms of its stiffness, strength, and thermal conductivity, among other mechanical and thermal performance aspects while the density is reduced. The fabrication of such attractive yet complex materials has become possible due to the witnessed advancements in fabrication techniques. However, a major challenge in adapting cellular solids in mechanical design is choosing the appropriate lattice design. Therefore, this paper focuses on studying the compressive mechanical behavior of four different types of cellular solids with topologies based on the mathematically known triply periodic minimal surfaces (TPMS); namely, Diamond (D), I-WP (IWP), Gyroid (G), and Fisher-Koch C(Y) (CY). These cellular materials are 3D printed using the powder bed fusion selective laser sintering technique out of Nylon thermoplastic polymer at various relative densities. The effects of the number of unit cells, type of the ligament-based TPMS architecture, and relative density on the stiffness, yield strength, ultimate strength, and toughness are thoroughly investigated. The results indicated that the effect of the architecture is stronger when the relative density is decreased. Also, the analyses showed that all the tested architectures were bending dominated implying that it could be best applied in shock absorbing and vibration mitigation applications.

1. Introduction

Cellular solids can be observed in natural materials such as bone and wood where their low density and architected microstructure make them weight-efficient and good load-bearing solids with desired multifunctional properties (Ref 1-3). Cellular solids have inspired many studies and are of interest in several industries due to their promising specific mechanical and physical properties (Ref 4-10). They are used in many applications, such as thermal insulation, lightweight structures, filtering, thermal management. (Ref 1, 5, 11).

Lattices are an attractive subset of cellular solids that comprise a well-defined and periodic unit cell and provide easy control of mechanical and physical properties by controlling the topology of the unit cell. The fabrication of lattices using different materials and length-scales is made possible by advancements in additive manufacturing techniques which allowed for better integration of lattices in structural and mechanical components (Ref 12-14). However, since the properties of lattices are mainly driven by their base material and geometrical features (i.e., cell size, cell topology, relative density (RD)…etc.) a major challenge in adapting lattices in mechanical design is choosing the appropriate lattice design. Therefore, understanding the material-topology-property relationship that describes mechanical properties as a function of the relative density and exhibited topology is a prerequisite to allowing product design with improved end-use properties.

In this work, we experimentally investigate the mechanical properties of four different ligament-based lattices with topologies based on the triply periodic minimal surfaces (TPMS), namely; Diamond (D-LTPMS), I-WP (IWP-LTPMS), Gyroid (G-LTPMS), and Fisher-Koch C(Y) (CY-LTPMS) where LTPMS stands for ligament-based TPMS. Minimal surfaces are defined as surfaces of zero mean curvature, meaning that the sum of the principal curvatures at each point is zero. Minimal is referred to a fixed boundary curve where the area of a ''minimal surface'' is minimal with respect to other surfaces with the same boundary. TPMS are minimal surfaces that can be repeated in 3D and have a crystalline structure (Ref 15) (see Fig. 1). Therefore, TPMS are infinite, periodic in three perpendicular directions, free of self-intersections, and have space group symmetry (Ref 16). These surfaces can be used to create lattices in two different ways to yield sheet-based and ligament-based lattices as shown by Kapfer et al. (Ref 17). Due to their attractive topological characteristics, several studies have established the material-topology-property relationship for a number of TPMS-based lattices and composites both experimentally and numerically (Ref 13, 18-34). Of interest, are the studies that investigated lattices fabricate using powder bed fusion (PBF) AM technique for being a mature and widely used technique for the fabrication of end-use products. For example, metallic sheet-based TPMS lattices (Ref 23, 35-37) and ligament-based (Ref 19, 38-43) TPMS lattices were

Aliaa M. Abou-Ali and **Oraib Al-Ketan**, Mechanical Engineering Department, Masdar Institute, Khalifa University of Science and Technology, Abu Dhabi, UAE; **Reza Rowshan**, Core Technology Platforms Division, New York University Abu Dhabi, Abu Dhabi, UAE; and **Rashid Abu Al-Rub**, Mechanical Engineering Department, Masdar Institute, Khalifa University of Science and Technology, Abu Dhabi, UAE; and Aerospace Engineering Department, Khalifa University of Science and Technology, Abu Dhabi, UAE. Contact emails: ogalketan@masdar.ac.ae, rashid.abualrub@ku.ac.ae and rashedkamel@yahoo.com.
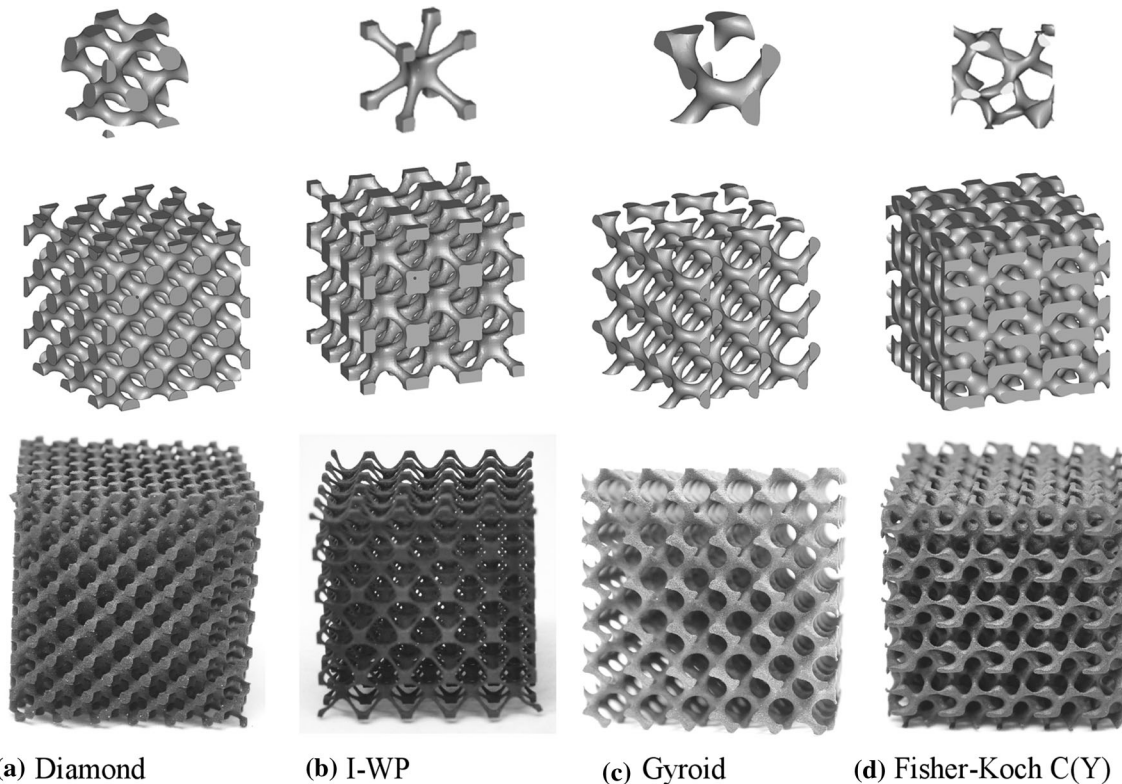
Fig. 1 TPMS-based lattices. (a) Diamond ligament-based TPMS, (b) IWP ligament-based TPMS, (c) Gyroid ligament-based TPMS, and (d) Fischer-Koch C(Y) ligament-based TPMS. Top row shows single unit cells, middle raw shows a 3 × 3 × 3 pattern CAD designs, and the bottom row shows 3D printed samples with 5 × 5 × 5 pattern

investigated for their compressive mechanical properties. However, there have been relatively few reports that established the material-topology-property of PBF-based polymeric TPMS lattices (Ref 20-22). Therefore, this study is the first instance of PBF additively manufactured polymeric Diamond, I-WP, Gyroid, and Fisher-Koch C(Y) lattices having been experimentally investigated together in a single investigation. We examine the compressive behavior of these lattice types and establish their topology-mechanical property relationship by comparing their respective stress–strain (SS) responses, uniaxial elastic moduli, yield strengths, compressive strengths, toughness, hardening modulus and exhibited deformation mechanism.

2. Materials and Methods

2.1 Design and Manufacturing

The TPMS ligament-based lattices have been mathematically created using level-set approximation equations (Ref 44). These equations consist of trigonometric functions that define an iso-surface of some function f that satisfies the equality $f(x, y, z) = 0$. For the TPMS, these functions are presented in Table 1. The constant t is used to control the volume fraction of the lattice. Table 2 shows the exact t value that was used to achieve a certain RD for each specific lattice topology. Plotting software was used to plot the functions and create the needed STL files for 3D printing. Each architecture was designed with
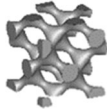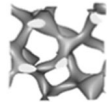
various relative densities in order to evaluate and compare their mechanical behavior.

Several G-LTPMS lattices with 10.5% RD were tested in order to investigate the effect of changing the number of unit cells on the obtained mechanical properties. It was concluded that a periodicity of 5 × 5 × 5 and a unit cell of 8 mm are enough to obtain the effective properties of the lattices (more details are provided in section 3.2). Thus, all lattices (D-LTPMS, IWP-LTPMS, G-LTPMS, and CY-LTPMS) were designed and printed at a 5 × 5 × 5 periodicity and 8 mm unit cell size at different RDs.

2.2 Fabrication of LTPMS Lattices

LTPMS lattices were fabricated using the powder bed fusion technology. In this technique, the base material is in the form of powder and it is evenly laid on a building platform. An energy source (laser) is used to melt the powder. The printing takes place in a layer by layer approach such that laser selectively melts the powder in the first layer, then, the building platform moves down and the second layer of powder is spread over the first layer. This process continues until the three-dimensional component is fully fabricated. For this purpose, the EOS Formiga P110 sintering system was employed, and the PA1102 polymeric black powder was used. PA1102 is a mass colored black polyamide powder made out of renewable raw materials (e.g., castor oil). In fact, PA1102 black is a thermoplastic material that has a similar behavior of Nylon. This material is characterized by high elasticity and high impact resistance and is suitable for small- to medium-sized components, and more importantly, lattice structures. Figure 2 shows SEM images of

Table 1 Mathematical level-set approximations of the designed TPMS architectures

TPMS lattice	Level-set approximation equation	Graphical representation
D	$(\cos 2\pi x * \cos 2\pi y * \cos 2\pi z) - (\sin 2\pi x * \sin 2\pi y * \sin 2\pi z) - t$	
IWP	$2[(\cos 2\pi x * \cos 2\pi y) + (\cos 2\pi y * \cos 2\pi z) + (\cos 2\pi z * \cos 2\pi x)]$ $- (\cos 4\pi x + \cos 4\pi y + \cos 4\pi z) - t$	
G	$(\sin 2\pi x * \cos 2\pi y) + (\sin 2\pi y * \cos 2\pi z) + (\sin 2\pi z * \cos 2\pi x) - t$	
CY	$- \sin 2\pi x * \sin 2\pi y * \sin 2\pi z + \sin 4\pi x * \sin 2\pi y + \sin 4\pi y * \sin 2\pi z + \sin 4\pi z * \sin 2\pi x$ $- \cos 2\pi x * \cos 2\pi y * \cos 2\pi z + \sin 4\pi x * \cos 2\pi z$ $+ \sin 4\pi y * \cos 2\pi x + \sin 4\pi z * \cos 2\pi y - t$	

Table 2 Offset values t corresponding to each designed RD for each architecture

D-LTPMS		IWP-LTPMS		G-LTPMS		CY-LTPMS	
RD, %	t value	RD, %	t value	RD, %	t value	RD, %	t value
10.3	0.67	7.2	2.79	6.1	1.30	9.8	1.76
14.0	0.61	12.6	2.57	10.8	1.16	13.0	1.63
17.8	0.55	17.3	2.35	15.3	1.04	16.0	1.50
21.4	0.49	21.5	2.11	19.6	0.92	19.1	1.37
25.1	0.43	25.4	1.89	23.9	0.80	22.0	1.25
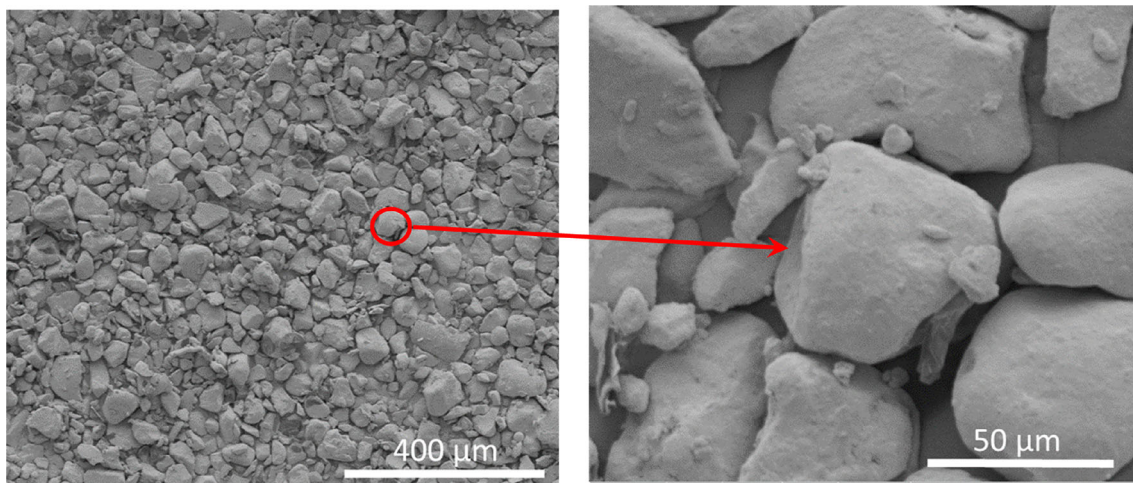
Fig. 2 SEM image of PA 1102 black fabricated by the 3D printer Formiga 110

the used powder where grains of powder have an irregular shape with an average size of approximately 50 μm. The size of the grains significantly affects the properties of the material and controls the dimensions and quality of the printed structures. After printing the samples, SEM was used to assess the quality of printing.

2.3 Uniaxial Compression Testing

Uniaxial compression tests were carried out to assess the compressive properties of the manufactured parts using the Universal Material Testing Machine INSTRON—5980 Series with a load cell of 100 kN. Two smooth steel plates which are polished and hardened were used to reduce friction in compression test and avoid nonhomogeneous deformation. The compression loading is measured and the displacement is obtained from the vertical movement of the crosshead until full densification of the specimen. The obtained stress–strain (SS) response is used to deduce the uniaxial modulus, yield strengths, compressive strengths, toughness, and hardening modulus. Due to the high repeatability, only two samples were tested for the same RD and architecture, where the mean and standard deviation were calculated for each part. The compression load was applied parallel to the printing direction.

It is noteworthy that there are other factors that could affect the mechanical behavior of polymers, such as the strain rate, aging effect, and temperature. These parameters are fixed in this study where the strain rate was set to 0.001/s, and samples were tested at room temperature 10 days after printing.

3. Results and Discussion

3.1 Manufacturability of LTPMS-Based Lattices

After printing, samples were air-weighted and their actual RD was calculated. Figure 3 plots the designed and actual RDs for all the printed samples. A clear deviation in the measured RD can be noted as compared to the designed RD. This deviation increases as the RD increase. As the RD increases, the surface area of the lattice increases as well, As such, more surface of interaction between the powder and the lattice is
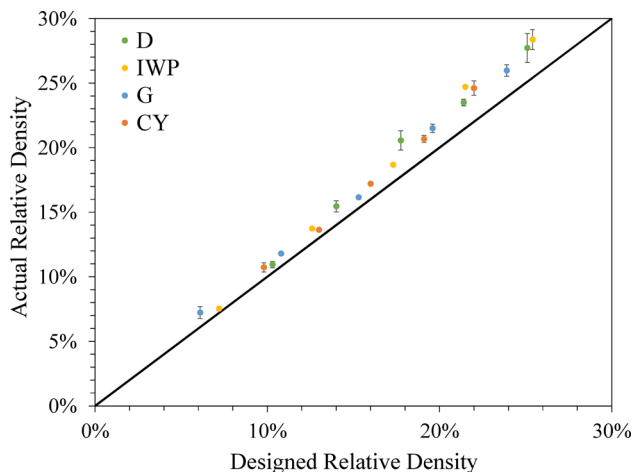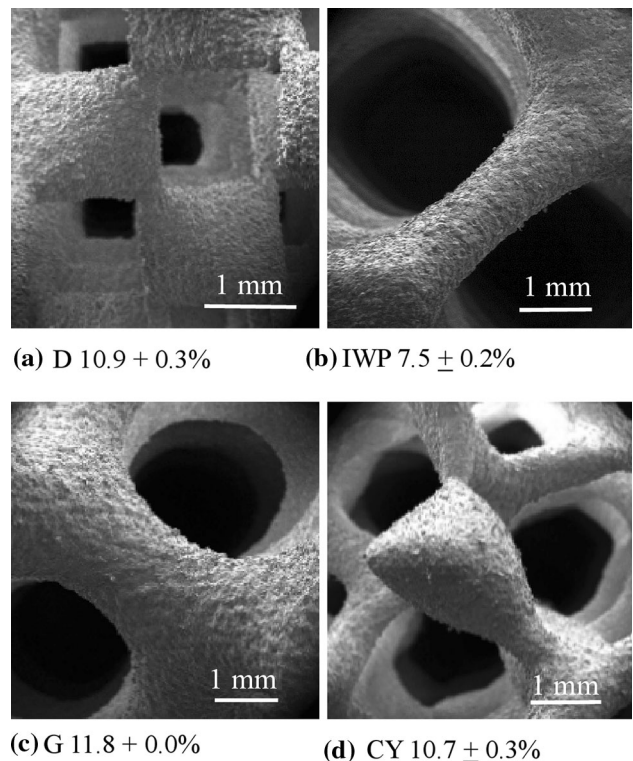
available. As a result, more powder adheres to the surface of the lattice which contributes to the added weight. The powder adhering to the surface of the lattice can be observed in the SEM images shown in Fig. 4. Powder adhesion can be attributed to difference in thermal diffusivity between the sintered part and the loose powder surrounding it. Also, the melt pool size of the contour track can be larger than the laser spot size, resulting in oversizing in the sintered part. Although the scan vectors of contour track are usually shifted inward to compensate for this possible deviation (Ref 45), it is still not enough to get the required precision. Moreover, the depth of the melt pool is slightly larger than the layer thickness to form overlaps between successive layers and ensure homogeneous fusion between layers, however, the curved components have layers that lay partially on powder, resulting in more fusion of powder and, ultimately, strut oversizing.

3.2 Periodicity and Effective Properties

Several Gyroid ligament-based TPMS architectures with 10.5% RD are tested in order to investigate the periodicity effect on SS responses. The periodicity effect was investigated by testing cubic samples with a different number of unit cells in the sample while fixing the unit cell size. For this purpose, the unit cell size was fixed to 8 mm and the periodicity was changed such that samples with 27, 64, 125, and 216 unit cells are tested as shown in Fig. 5(a). SS responses of the tested samples are plotted in Fig. 5(b). The responses of the different periodicities showed a similar behavior where a linear elastic

Fig. 3 Designed relative density vs. actual relative density for different ligament-based TPMS (Diamond, I-WP, Gyroid, and Fischer-Koch C(Y))

(a) D 10.9 + 0.3% **(b)** IWP 7.5 ± 0.2%

(c) G 11.8 + 0.0% **(d)** CY 10.7 ± 0.3%

Fig. 4 SEM images of different SLS 3D printed samples, (a) Diamond ligament-based TPMS with 10.9 + 0.3% relative density, (b) I-WP ligament-based TPMS with 7.5 + 0.2% relative density, (c) Gyroid ligament-based TPMS with 11.8 + 0.0% relative density, (d) Fischer-Koch C(Y) ligament-based TPMS with 10.7 + 0.3% relative density
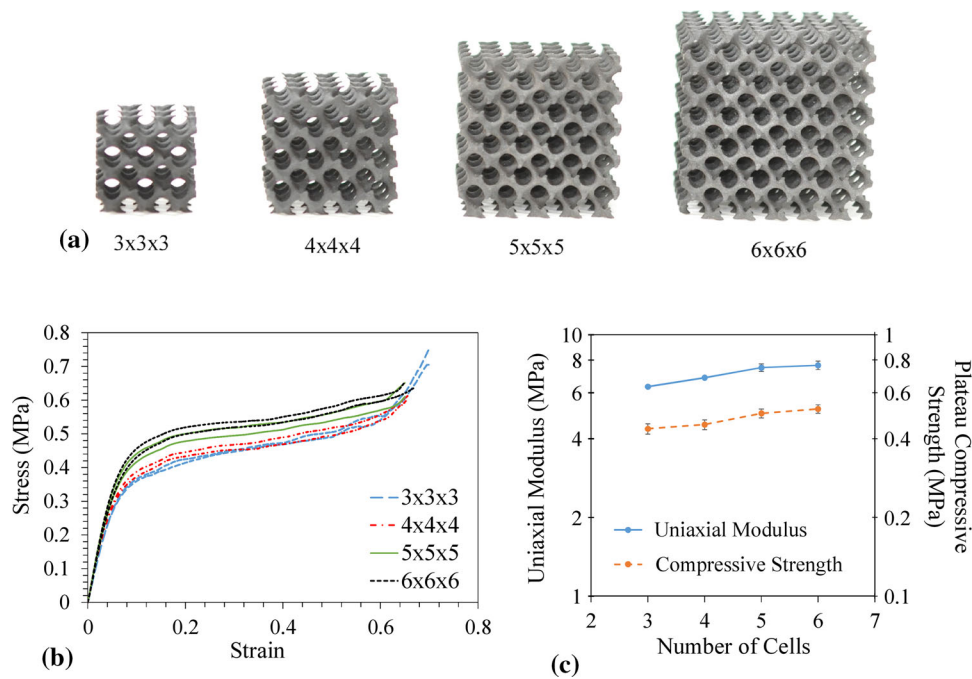
Fig. 5 Periodicity effect analysis for Gyroid ligament-based TPMS. (a) Show samples with different periodicities. (b) SS response of the tested samples at different periodicities. (c) Uniaxial modulus and plateau compressive strength deduced from the SS responses and plotted against the periodicity

**Table 3 Designed vs. actual RD for samples used in the periodicity study**

Periodicity	Designed RD, %	Actual RD		Average actual RD, %
		Sample 1, %	Sample 2, %	
Extrinsic size effect				
3 × 3 × 3	10.5	12.35	12.52	12.44
4 × 4 × 4	10.5	12.77	12.24	12.50
5 × 5 × 5	10.5	12.35	12.71	12.53
6 × 6 × 6	10.5	12.35	12.30	12.33

region is followed by a plastic region that extends from the yield strength up to the densification. This plastic part takes the shape of a plateau with a slope that defines the hardening behavior of the sample under compression. Although a similar SS response is observed for all the tested samples, the mechanical properties seem to increase as the number of unit cells increase. This increase in mechanical properties seems less pronounced when periodicity reaches five unit cells and above, where the SS curves tend to overlap indicating that a periodicity of five unit cells can be enough to obtain the effective properties. This was quantitatively demonstrated by analyzing the uniaxial modulus and plateau strength (defined as the average stress for the strain range 20-30%) of the tested samples as presented in Fig. 5(c). In this figure, the difference in absolute values between the 3 × 3 × 3 periodicity and 4 × 4 × 4 periodicity is higher than that between 4 × 4 × 4 and 5 × 5 × 5 and this difference between successive periodicities keeps decreasing as periodicity increases to reach less than 3% between the 5 × 5 × 5 and 6 × 6 × 6 periodicity. Even this < 3% difference might be attributed to the slight difference in the obtained RD which are presented in Table 3. Therefore, it can be assumed that a periodicity of 5 unit cells is

sufficient to obtain the effective mechanical properties. It is noteworthy that these conclusions are based on the Gyroid Ligament-based TPMS only at a relative density of 10.5%, and they may not be necessarily accurate for the other relative densities and lattice topologies. However, other numerical analysis for different TPMS-based cell topologies suggested the suitability of such periodicity (Ref 20). In fact, Ashby et al. (Ref 46) concluded that a periodicity of more than 7 × 7 × 7 unit cells is sufficient to obtain effective properties for metallic cellular materials, which is consistent with the current conclusion for polymeric cellular materials.

3.3 Relative Density and Architecture Effect

The effect of changing both the architecture and the relative densities of the Ligament-based TPMS are experimentally investigated. Figure 6 shows the typical compressive SS response for each unit cell topology at different relative densities, and comparison between them. All the tested samples showed a typical cellular material's compressive SS response as observed previously in the periodicity study. Again, all the samples exhibited a linear elastic response followed by a plastic
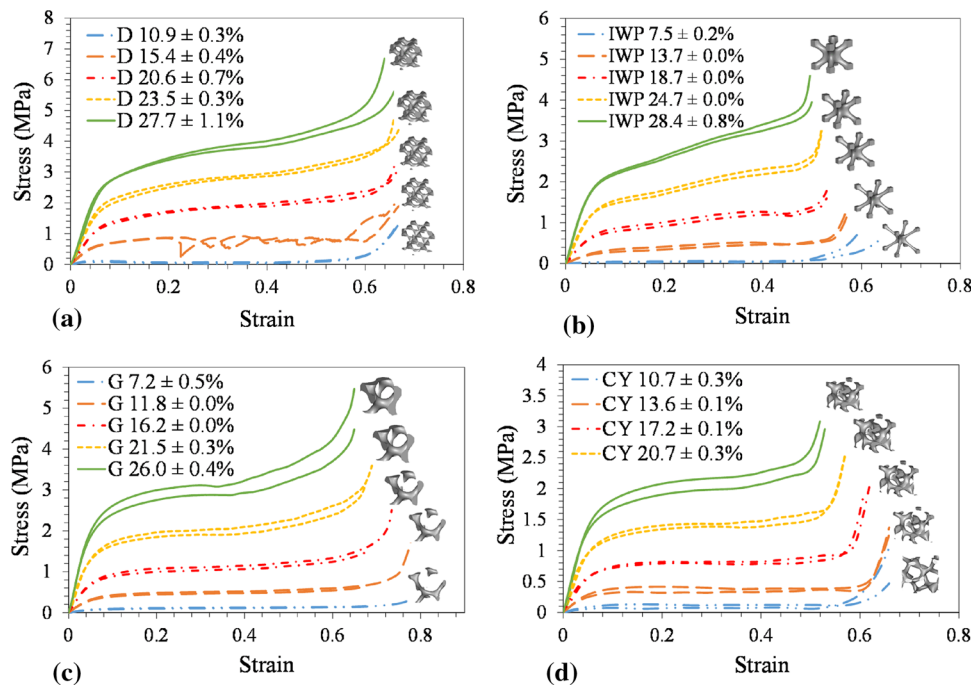
Fig. 6 Stress–strain responses for the ligament-based TPMS at different relative densities (a) D-LTPMS, (b) IWP-LTPMS, (c) G-LTPMS, and (d) CY-LTPMS

region that extends from the yield strength up to the densification. The plateau region shows a smooth SS response without noticeable stress fluctuations which is a behavior that can be linked to the nature of the constituent material. For example, the smooth plateau stress response observed in the current study for the Diamond lattice is much different than what was observed in the studies of Al-Ketan et al. (Ref 23) or Yan et al. (Ref 40) both of which were performed on metallic materials. Al-Ketan et al. (Ref 23) studied the compressive mechanical properties of different TPMS-based lattices made of Maraging steel and reported their SS responses. In that study, the ligament-based Diamond lattice exhibited a catastrophic drop in the SS curve right after the maximum strength is reached, this drop was related to the failure of the first layer of unit cells. The same behavior was observed for the Diamond lattice made of AlSi10 Mg (Aluminum alloy) investigated by Yan et al. (Ref 40). On the other hand, the Gyroid lattice was also investigated for its compressive properties using a range of materials such Maraging steel (Ref 23), Aluminum alloy, Titanium alloy (Ref 38), and Stainless steel (Ref 42) where the SS response shows a similar behavior as obtained in the current study except for small fluctuations observed while using Titanium alloy (Ref 38). Similarly, the IWP was investigated for its compressive properties using Maraging steel (Ref 23) and Titanium alloy (Ref 19) where small fluctuation in the SS responses are observed especially at high RD. In general, fluctuations in the SS response can be linked to the onset of fracture of some of the ligaments, while a smooth plateau stress may indicate that the ligaments are undergoing plastic deformation without severe fracturing of ligaments. Figure 7 shows the deformation patterns of the different lattices under different strain levels. The figure shows that samples undergo a uniform deformation where the struts tend to rotate around their nodes to accommodate the applied load. This behavior is different than what is

commonly observed in metallic lattices where shear bands may form first (Ref 23, 24, 47).

The mechanical properties (modulus, yield strength, compressive strength, toughness, and plateau stress) of each LTPMS architecture are deduced from SS responses and plotted as a function of the relative density in Fig. 8. Two samples for each LTPMS were tested at five different relative densities to establish reliability. The uniaxial modulus was determined by the slope of the elastic region before yielding, the yield strength was determined by the intersect of a parallel line to the slope of the elastic region at an offset of 1% compressive strain, the compressive strength is the maximum strength reached before densification (60% compressive strain), the toughness is the area under the curve until densification, and the plateau stress is calculated as the mean of the stresses between 20 and 30% compressive strain (Ref 35). From Fig. 8, it could be observed that the G-LTPMS has the highest mechanical properties in terms of Young's modulus, yield strength, compressive strength, toughness, and plateau stress. However, at higher RDs, the D-LTPMS starts to have higher mechanical properties as compared to the other lattices including the G-LTPMS. This can be attributed to the cross-sectional area of the nodes at which the ligaments of the D-LTPMS lattices intersect. At small RDs, these nodes are small as can be seen in the SEM images in Fig. 2 where the cross-sectional area of the D (at RD of 10.9 ± 0.3%) is approximately 300 μm and can be susceptible to stress concentrations. In fact, at small RDs, the mechanical properties of the D-LTPMS are the least as compared to other lattices; however, as the RD increases the cross-sectional area of these nodes increase and their curvature becomes more apparent such that stress concentrations are reduced. It can also be observed in Fig. 8 that the mechanical properties of the four lattices tend to converge at high RDs which suggests that the role of
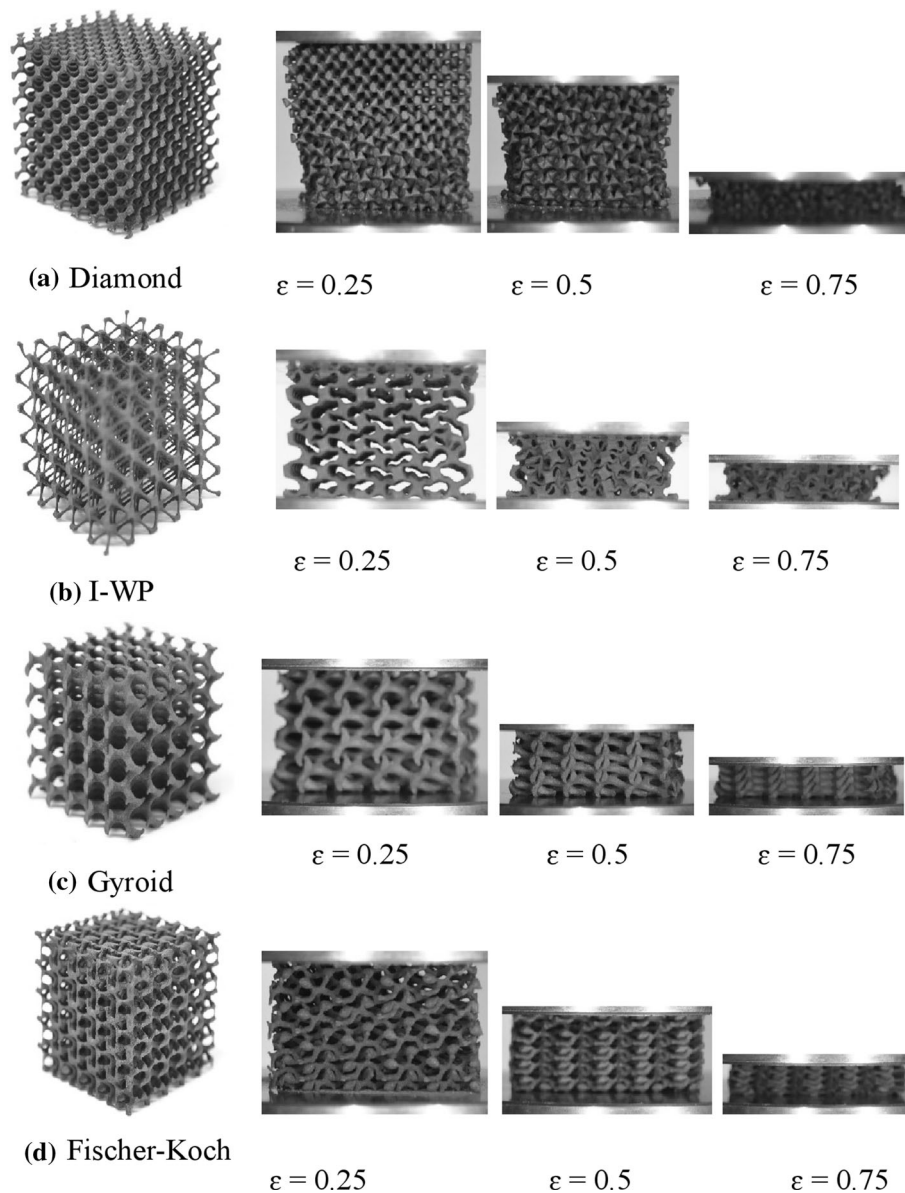
Fig. 7 Deformation patterns of the different lattices at different strain levels. (a) Diamond, (b) I-WP, (c) Gyroid, and (d) Fischer-Koch C(Y) ligament-based TPMS

architecture is more pronounced at lower RD, where at higher RDs the properties of the base material become more dominating and reduce the architecture effect. Overall, at high RD, the Diamond and Gyroid have the highest uniaxial modulus and almost the same values. The Diamond also has the highest yield strength and compressive strength. In terms of toughness, the I-WP has the highest toughness.

The deduced mechanical properties as a function of the RD are fitted using a power law in the form of (Ref 1):

$$M = C\bar{\rho}^n \qquad \text{(Eq 1)}$$

where M is the mechanical property, $\bar{\rho}$ is the relative density, and C and n are fitting constants. The prefactor C is a geometrical parameter and its value is altered by the material distribution within the unit cell. On the other hand, the scaling exponent n indicates the mode of deformation. A value of n less than 2 for the modulus and less than 1.5 for the strength denotes stretching dominating deformation, while a value greater than 2

for the modulus and greater than 1.5 for the strength denotes bending-dominating deformation (Ref 1). Commonly, stretching dominating architectures have higher elastic modulus and yield strength than the bending-dominating architectures. But, on the other hand, bending-dominating architectures can sustain larger strains, which could be best implemented in high energy absorption applications such as impact resistance, vibration damping, and energy dissipation.

As mentioned earlier, it could be clearly observed that at low relative densities the superiority of the G-LTPMS over the other architectures. The G-LTPMS has the best mechanical properties in terms of the uniaxial modulus, yield strength, compressive strength, and toughness, which makes it a very promising architecture; however, the exponent is still in the order of 2, meaning that it is a bending-dominated lattice. In fact, it could be observed from Table 4 that all the exponent values of modulus are greater than 2 and the strength is greater than 1.5, which implies that the deformation mode of all of the currently
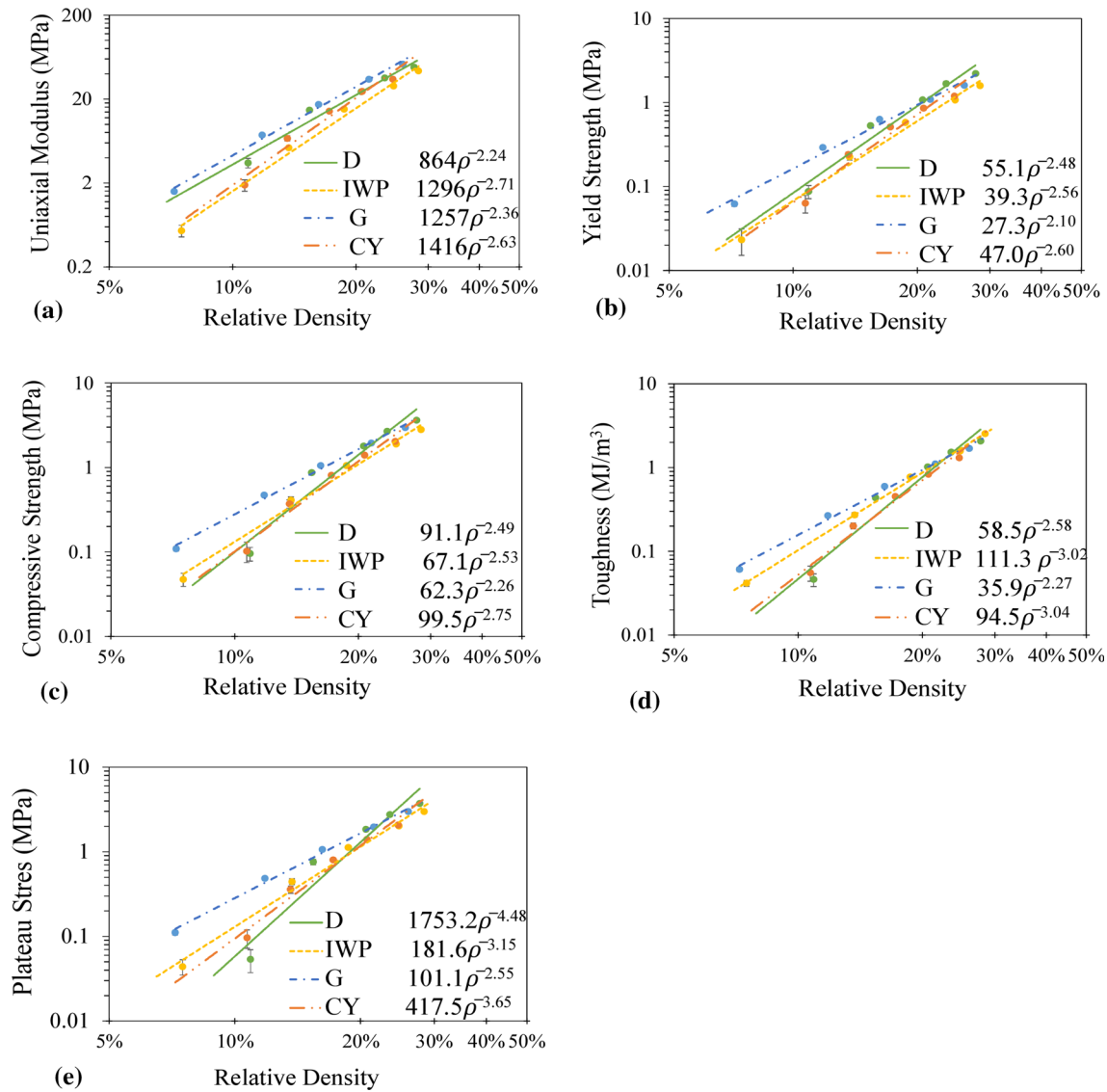
Fig. 8 Mechanical properties of the ligament-based TPMS (D, IWP, G, and CY). (a) Uniaxial modulus, (b) yield strength, (c) compressive strength, (d) toughness, and (e) plateau stress

**Table 4 Summary of fitting constants of the mechanical properties using the power law in Eq. (1)**

	Uniaxial modulus, MPa		Yield strength, MPa		Compressive strength, MPa		Toughness, MJ/m³		Plateau stress, MPa	
	C, MPa	**n**	**C, MPa**	**n**	**C, MPa**	**n**	**C, MPa**	**n**	**C, MPa**	**n**
Fitting constants										
D-LTPMS	864	2.24	55.1	2.48	91.1	2.49	58.5	2.58	1753.2	4.48
IWP-LTPMS	1296	2.71	39.3	2.56	67.1	2.53	111.3	3.02	181.6	3.15
G-LTPMS	1257	2.36	27.3	2.10	62.3	2.26	35.9	2.27	101.1	2.55
CY-LTPMS	1416	2.63	47.0	2.60	99.5	2.75	94.5	3.04	417.5	3.65

investigated architectures is bending dominated under uniaxial compression. In a bending-dominated mode of deformation, struts/ligaments deform either in bending, twisting, or buckling of the struts unlike the stretching-dominated mode of deformation where struts experience mainly axial loading (tension or compression). In Fig. 9, we present a closer view of the

deformation patterns presented in Fig. 7. It can be observed that ligaments are bending and rotating around their connecting nodes confirming the hypothesis of bending-dominated deformation mode.

Another important aspect that was taken into consideration is the sample's deformation recoverability. This was achieved
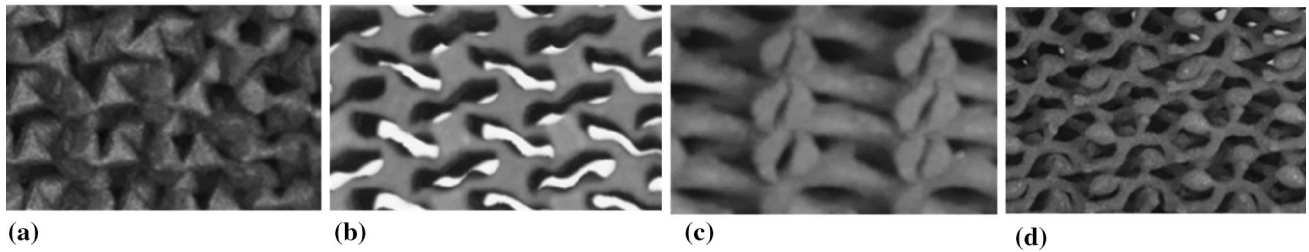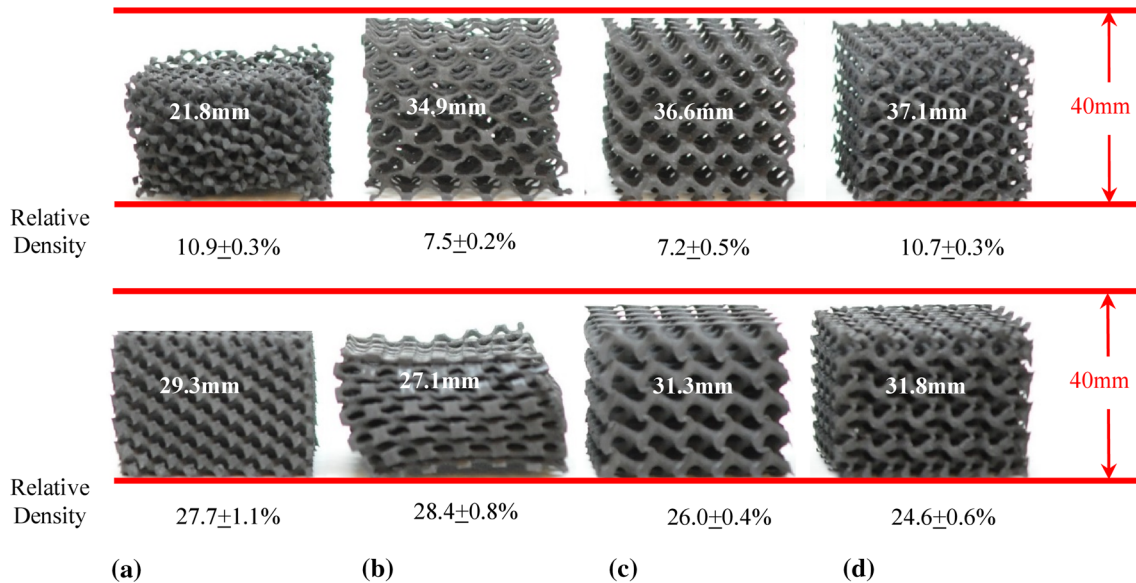
Fig. 9 The behavior of struts in bending-dominating lattices subjected to compressive loading. (a) D-LTPMS, (b) IWP-LTPMS, (c) G-LTPMS, and (d) CY-LTPMS
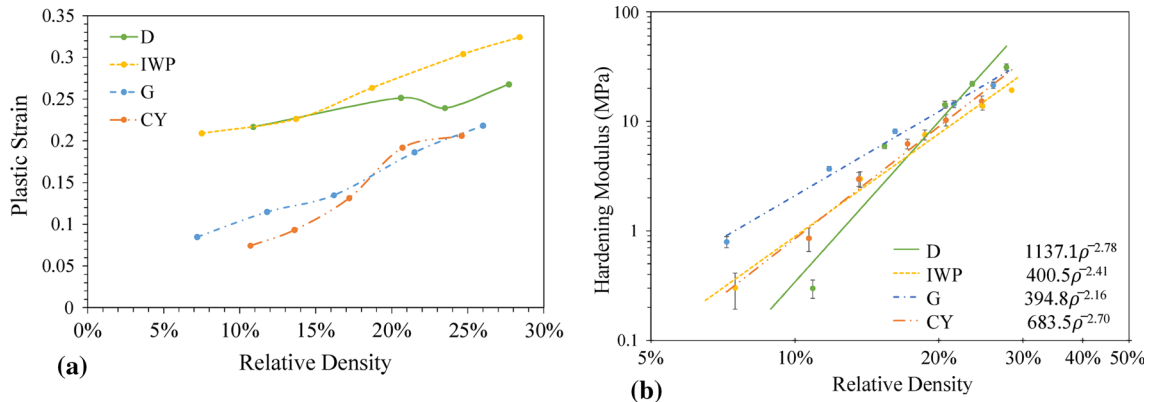
Fig. 10 (a) Plastic strain, and (b) hardening modulus for the ligament-based TPMS

Fig. 11 Comparing the original height (40 mm) with the final height of the tested specimens showing the plastic deformation, the top image is for the high relative densities and the bottom image is for the low relative densities. (a) D-LTPMS, (b) IWP-LTPMS, (c) G-LTPMS, and (d) CY-LTPMS

by observing the deformation process and measuring the plastic strain of each architecture after the uniaxial compression test. Figure 10(a) and (b) shows the plastic strain and hardening modulus for the ligament-based TPMS. The hardening modulus is the plastic behavior of the architecture, which is captured by the slope of the SS curve between initial yielding and densification. The hardening modulus is calculated to measure the resistance of the architecture to deformation such that the steeper the slope the more resistant to deformation. While the plastic strain is the amount of strain that remains in the sample after unloading and is calculated by the difference between the original height and the height after unloading divided by the

original height. The lower the plastic strain, the higher the hardening modulus and the recoverability. It could be observed that the lower the RD, the lower the plastic strain and the higher the recoverability as can be noted in Fig. 10(a). However, the D-LTPMS had the lowest recoverability of around 55% (see Fig. 11) and highest plastic strain at low RD. The D-LTPMS at low RD experienced several fracture events within its ligaments due to its smaller cross-sectional area at depths where fractures initiate. On the other hand, although the CY-LTPMS also had a small cross-sectional area (diameter of approximately 530 μm) the ligaments did not experience fracturing at low RD (10.7 ± 0.3%) and had the highest recoverability of almost 93%. Nevertheless, the G-LTPMS and IWP-LTPMS had relatively high recoverability of almost 92 and 88%, respectively, at low RDs (7.2 ± 0.5 and 7.5 ± 0.2%). However, the IWP-LTPMS became stiffer at high RD (28.4 ± 0.8%) as it had the highest plastic strain, hence lowest hardening modulus and recoverability of almost 68%.

4. Conclusions

In this paper, the compressive mechanical behavior of four polymeric ligament-based TPMS (Diamond, I-WP, Gyroid, and Fischer-Koch C(Y)) was experimentally investigated at different relative densities. These architectures were printed using powder bed fusion—selective laser sintering, and their microstructures were characterized using SEM imaging. The effective properties were investigated under uniaxial compression. It was concluded that five unit cells were sufficient to obtain the effective (macroscopic) mechanical properties. The mechanical properties (uniaxial modulus, yield strength, compressive strength, and toughness) of the investigated lattices were deduced from the stress–strain responses. Results indicated that the Gyroid lattice had the best mechanical properties and are favorable at low relative densities. The Diamond and Fischer-Koch C(Y) lattices had the least mechanical properties due to their weak and small cross-sectional area at the connecting nodes. Nevertheless, it was observed that at high relative densities the mechanical properties of all the architectures converge and become closer indicating that the effect of architecture is stronger when the relative density is decreased. It was concluded that the Gyroid and the Fischer-Koch C(Y) had the highest deformation recoverability at low and high relative densities when compared to the other architectures. All the investigated lattices exhibited a bending-dominated mode of deformation implying that they are ideal for energy absorption applications.

References

1. L.J. Gibson and M.F. Ashby, *Cellular Solids: Structure And Properties*, Cambridge University Press, Cambridge, 1999

2. M. Ashby, The Properties of Foams and Lattices, *Philos. Trans. R. Soc. Lond. A: Math. Phys. Eng. Sci.*, 2006, **364**(1838), p 15–30

3. V. Deshpande, M. Ashby, and N. Fleck, Foam Topology: Bending Versus Stretching Dominated Architectures, *Acta Mater.*, 2001, **49**(6), p 1035–1040

4. S. Guessasma, P. Babin, G. Della Valle, and R. Dendievel, Relating Cellular Structure of Open Solid Food Foams to Their Young's Modulus: Finite Element Calculation, *Int. J. Solids Struct.*, 2008, **45**(10), p 2881–2896

5. W. Lee, Cellular Solids, Structure and Properties, *Mater. Sci. Technol.*, 2000, **16**(2), p 233

6. M.K. Ravari, M. Kadkhodaei, M. Badrossamay, and R. Rezaei, Numerical Investigation on Mechanical Properties of Cellular Lattice Structures Fabricated by Fused Deposition Modeling, *Int. J. Mech. Sci.*, 2014, **88**, p 154–161

7. V. Valuiskikh, Method of Stochastic Simulation Modeling of the Structure, Calculation, and Optimization of the Physicomechanical Characteristics of Foam Plastics, *Mech. Compos. Mater.*, 1990, **25**(4), p 429–435

8. V. Yakushin and U. Stirna, Physicomechanical Characteristics of Spray-on Rigid Polyurethane Foams at Normal and Low Temperatures, *Mech. Compos. Mater.*, 2002, **38**(3), p 273–280

9. R. Gümrük, R. Mines, and S. Karadeniz, Determination of Strain Rate Sensitivity of Micro-struts Manufactured Using the Selective Laser Melting Method, *J. Mater. Eng. Perform.*, 2018, **27**(3), p 1016–1032

10. M.K. Ravari and M. Kadkhodaei, A Computationally Efficient Modeling Approach for Predicting Mechanical Behavior of Cellular Lattice Structures, *J. Mater. Eng. Perform.*, 2015, **24**(1), p 245–252

11. T. Lu, H. Stone, and M. Ashby, Heat Transfer in Open-Cell Metal Foams, *Acta Mater.*, 1998, **46**(10), p 3619–3635

12. L.R. Meza, S. Das, and J.R. Greer, Strong, Lightweight, and Recoverable Three-Dimensional Ceramic Nanolattices, *Science*, 2014, **345**(6202), p 1322–1326

13. O. Al-Ketan, R. Rezgui, R. Rowshan, H. Du, N.X. Fang, and R.K. Abu Al-Rub, Microarchitected Stretching-Dominated Mechanical Metamaterials with Minimal Surface Topologies, *Adv. Eng. Mater.*, 2018, **20**(9), p 1800029

14. X. Zheng, W. Smith, J. Jackson, B. Moran, H. Cui, D. Chen, J. Ye, N. Fang, N. Rodriguez, T. Weisgraber, and C.M. Spadaccini, Multiscale Metallic Metamaterials, *Nat. Mater.*, 2016, **15**, p 1100

15. A.H. Schoen, Infinite Periodic Minimal Surfaces Without Self-Intersections, NASA Report D5541, 1970

16. D. Cvijović and J. Klinowski, The Computation of the Triply Periodic I-WP Minimal Surface, *Chem. Phys. Lett.*, 1994, **226**(1), p 93–99

17. S.C. Kapfer, S.T. Hyde, K. Mecke, C.H. Arns, and G.E. Schröder-Turk, Minimal Surface Scaffold Designs for Tissue Engineering, *Biomaterials*, 2011, **32**(29), p 6875–6882

18. M. Afshar, A.P. Anaraki, H. Montazerian, and J. Kadkhodapour, Additive Manufacturing and Mechanical Characterization of Graded Porosity Scaffolds Designed Based on Triply Periodic Minimal Surface Architectures, *J. Mech. Behav. Biomed. Mater.*, 2016, **62**, p 481–494

19. J. Kadkhodapour, H. Montazerian, A.C. Darabi, A. Zargarian, and S. Schmauder, The Relationships Between Deformation Mechanisms and Mechanical Properties of Additively Manufactured Porous Biomaterials, *J. Mech. Behav. Biomed. Mater.*, 2017, **70**, p 28–42

20. I. Maskery, A.O. Aremu, L. Parry, R.D. Wildman, C.J. Tuck, and I.A. Ashcroft, Effective Design and Simulation of Surface-Based Lattice Structures Featuring Volume Fraction and Cell Type Grading, *Mater. Des.*, 2018, **155**, p 220–232

21. I. Maskery, L. Sturm, A.O. Aremu, A. Panesar, C.B. Williams, C.J. Tuck, R.D. Wildman, I.A. Ashcroft, and R.J.M. Hague, Insights into the Mechanical Properties of Several Triply Periodic Minimal Surface Lattice Structures Made by Polymer Additive Manufacturing, *Polymer*, 2018, **152**, p 62–71

22. D.W. Abueidda, M. Bakir, R.K. Abu Al-Rub, J.S. Bergström, N.A. Sobh, and I. Jasiuk, Mechanical Properties of 3D Printed Polymeric Cellular Materials with Triply Periodic Minimal Surface Architectures, *Mater. Des.*, 2017, **122**, p 255–267

23. O. Al-Ketan, R. Rowshan, and R.K. Abu Al-Rub, Topology-Mechanical Property Relationship of 3D Printed Strut, Skeletal, and Sheet Based Periodic Metallic Cellular Materials, *Addit. Manuf.*, 2018, **19**, p 167–183

24. O. Al-Ketan, R.K. Abu Al-Rub, and R. Rowshan, The Effect of Architecture on the Mechanical Properties of Cellular Structures Based on the IWP Minimal Surface, *J. Mater. Res.*, 2018, **33**(03), p 343–359

25. C. Yan, L. Hao, A. Hussein, and P. Young, Ti-6Al-4 V Triply Periodic Minimal Surface Structures for Bone Implants Fabricated via Selective Laser Melting, *J. Mech. Behav. Biomed. Mater.*, 2015, **51**, p 61–73

26. D.W. Abueidda, R.K. Abu Al-Rub, A.S. Dalaq, D.-W. Lee, K.A. Khan, and I. Jasiuk, Effective Conductivities and Elastic Moduli of Novel Foams with Triply Periodic Minimal Surfaces, *Mech. Mater.*, 2016, **95**, p 102–115

27. D.W. Abueidda, A.S. Dalaq, R.K. Abu Al-Rub, and H.A. Younes, Finite Element Predictions of Effective Multifunctional Properties of Interpenetrating Phase Composites with Novel Triply Periodic Solid Shell Architectured Reinforcements, *Int. J. Mech. Sci.*, 2015, **92**, p 80–89

28. A.S. Dalaq, D.W. Abueidda, and R.K. Abu Al-Rub, Mechanical Properties of 3D Printed Interpenetrating Phase Composites with Novel Architectured 3D Solid-Sheet Reinforcements, *Compos. A Appl. Sci. Manuf.*, 2016, **84**, p 266–280

29. O. Al-Ketan, M. Adel Assad, and R.K. Abu Al-Rub, Mechanical Properties of Periodic Interpenetrating Phase Composites with Novel Architected Microstructures, *Compos. Struct.*, 2017, **176**, p 9–19

30. O. Al-Ketan, R.K. Abu Al-Rub, and R. Rowshan, Mechanical Properties of a New Type of Architected Interpenetrating Phase Composite Materials, *Adv. Mater. Technol.*, 2017, **2**(2), p 1600235

31. O. Al-Ketan, A. Soliman, A.M. AlQubaisi, and R.K. Abu Al-Rub, Nature-Inspired Lightweight Cellular Co-Continuous Composites with Architected Periodic Gyroidal Structures, *Adv. Eng. Mater.*, 2018, **20**(2), p 1700549

32. K.A. Khan and R.K. Abu Al-Rub, Time Dependent Response of Architectured Neovius Foams, *Int. J. Mech. Sci.*, 2017, **126**, p 106–119

33. K.A. Khan and R.K. Abu Al-Rub, Modeling Time and Frequency Domain Viscoelastic Behavior of Architectured Foams, *J. Eng. Mech.*, 2018, **144**(6), p 04018029

34. D.-W. Lee, K.A. Khan, and R.K. Abu Al-Rub, Stiffness and Yield Strength of Architectured Foams Based on the Schwarz Primitive Triply Periodic Minimal Surface, *Int. J. Plast.*, 2017, **95**, p 1–20

35. F. Bobbert, K. Lietaert, A. Eftekhari, B. Pouran, S. Ahmadi, H. Weinans, and A. Zadpoor, Additively Manufactured Metallic Porous Biomaterials Based on Minimal Surfaces: A Unique Combination of Topological, Mechanical, and Mass Transport Properties, *Acta Biomater.*, 2017, **53**, p 572–584

36. I. Maskery, N.T. Aboulkhair, A.O. Aremu, C.J. Tuck, and I.A. Ashcroft, Compressive Failure Modes and Energy Absorption in Additively Manufactured Double Gyroid Lattices, *Addit. Manuf.*, 2017, **16**, p 24–29

37. L. Zhang, S. Feih, S. Daynes, S. Chang, M.Y. Wang, J. Wei, and W.F. Lu, Energy Absorption Characteristics of Metallic Triply Periodic Minimal Surface Sheet Structures Under Compressive Loading, *Addit. Manuf.*, 2018, **23**, p 505–515

38. A. Ataee, Y. Li, D. Fraser, G. Song, and C. Wen, Anisotropic Ti-6Al-4 V Gyroid Scaffolds Manufactured by Electron Beam Melting (EBM) for Bone Implant Applications, *Mater. Des.*, 2018, **137**, p 345–354

39. C. Han, Y. Li, Q. Wang, S. Wen, Q. Wei, C. Yan, L. Hao, J. Liu, and Y. Shi, Continuous Functionally Graded Porous Titanium Scaffolds Manufactured by Selective Laser Melting for Bone Implants, *J. Mech. Behav. Biomed. Mater.*, 2018, **80**, p 119–127

40. C. Yan, L. Hao, A. Hussein, S.L. Bubb, P. Young, and D. Raymont, Evaluation of Light-Weight AlSi10 Mg Periodic Cellular Lattice Structures Fabricated via Direct Metal Laser Sintering, *J. Mater. Process. Technol.*, 2014, **214**(4), p 856–864

41. C. Yan, L. Hao, A. Hussein, and D. Raymont, Evaluations of Cellular Lattice Structures Manufactured Using Selective Laser Melting, *Int. J. Mach. Tools Manuf.*, 2012, **62**, p 32–38

42. C. Yan, L. Hao, A. Hussein, P. Young, and D. Raymont, Advanced Lightweight 316L Stainless Steel Cellular Lattice Structures Fabricated via Selective Laser Melting, *Mater. Des.*, 2014, **55**, p 533–541

43. A. Yánez, A. Cuadrado, O. Martel, H. Afonso, and D. Monopoli, Gyroid Porous Titanium Structures: A Versatile Solution to be Used as Scaffolds in Bone Defect Reconstruction, *Mater. Des.*, 2018, **140**, p 21–29

44. K. Michielsen and J. Kole, Photonic Band Gaps in Materials with Triply Periodic Surfaces and Related Tubular Structures, *Phys. Rev. B*, 2003, **68**(11), p 115107

45. S. Van Bael, G. Kerckhofs, M. Moesen, G. Pyka, J. Schrooten, and J.-P. Kruth, Micro-CT-Based Improvement of Geometrical and Mechanical Controllability of Selective Laser Melted Ti-6Al-4 V Porous Structures, *Mater. Sci. Eng. A*, 2011, **528**(24), p 7423–7431

46. M.E. Ashby, A.G. Evans, N.A. Fleck, L.J. Gibson, J.W. Hutchinson, H.N.G. Wadley, Chapter 3: Characterization Methods 2000, *Metal Foams*, p 24–39

47. I. Maskery, N.T. Aboulkhair, A.O. Aremu, C.J. Tuck, I.A. Ashcroft, R.D. Wildman, and R.J.M. Hague, A Mechanical Property Evaluation of Graded Density Al-Si10-Mg Lattice Structures Manufactured by Selective Laser Melting, *Mater. Sci. Eng. A*, 2016, **670**, p 264–274

Publisher's Note Springer Nature remains neutral with regard to jurisdictional claims in published maps and institutional affiliations.